# Non-Conforming Nitsche Interfaces for Edge Elements in Curl–Curl-Type Problems

K. Roppert, S. Schoder, F. Toth, and M. Kaltenbacher

Institute for Mechanics and Mechatronics, TU Wien, 1060 Vienna, Austria

**In this article, a methodology to incorporate non-conforming interfaces between several conforming mesh regions is presented for Maxwell's curl–curl problem. The derivation starts from a general interior penalty discontinuous Galerkin formulation of the curl–curl problem and eliminates all interior jumps in the conforming parts but retains them across non-conforming interfaces. Therefore, it is possible to think of this Nitsche approach for interfaces as a specialization of discontinuous Galerkin on meshes, which are conforming nearly everywhere. The applicability of this approach is demonstrated in two numerical examples, including parameter jumps at the interface. A convergence study is performed for h-refinement, including the investigation of the penalization- (Nitsche-) parameter.**

*Index Terms*— **Eddy current problem, magnetostatic, Nédélec elements, Nitsche method, non-conforming interface.**

## I. Introduction

IN MANY technical applications, we encounter a field solution with locally concentrated behavior, which has to be resolved with a fine finite-element (FE) mesh, immersed in a surrounding region, where the mesh can be significantly coarser. Such problems can be handled efficiently via non-conforming interfaces. Also, the field of electrical machines makes use of these kinds of interfaces between the stator and rotor. There are several approaches to handling these interfaces. One way is to use interpolation between the quantities on both sides of the mesh, which is well investigated for rotating (sliding) interfaces of electrical machines, e.g., in [1] and [2]. Another concept consists of introducing additional degrees of freedom (dof) along with the interface in the form of Lagrange multipliers, representing the flux of the primary unknown, which means that the strong continuity of the primary unknown is replaced by a weak one. These methods are called Mortar methods. Originally introduced for coupling of spectral and FE methods [3], the analysis of Mortar methods has been extended to 3-D problems, together with advances in efficiently solving these types of problems (see [4]). Toward 3-D electromagnetics, special care has to be taken to achieve appropriate Lagrange multipliers, as described in [5] and [6] as well as [7] for electrical machines.

In this article, a different approach is used, based on the original idea of Nitsche [8] to incorporate Dirichlet boundary conditions into the weak form, which is also the starting point for many well researched discontinuous Galerkin (DG) methods. In general, there are two main DG methods: interior penalty (IP) and local discontinuous Galerkin (LDG), which appear in a large manifold of different flavors. For 2-D eddy current problems, an LDG approach was presented in [9], where the method was applied to the TEAM24 problem. In [10], the methodology was extended and analyzed for 3-D time-harmonic eddy current problems.

The focus of this article is to extend the IP approach from [11] by investigating and comparing the convergence behavior for edge elements of the first and second kinds. This article solely focuses on edge elements, using Nédélec basis functions and hierarchical polynomials, from [12], to discretize the continuous $H(\mathrm{curl}, \Omega)$ function space, needed for constructing the Nitsche approach.

Manuscript received December 19, 2019; revised February 9, 2020; accepted March 9, 2020. Date of publication March 12, 2020; date of current version April 17, 2020. Corresponding author: K. Roppert (e-mail: klaus.roppert@tuwien.ac.at).

Color versions of one or more of the figures in this article are available online at http://ieeexplore.ieee.org.

Digital Object Identifier 10.1109/TMAG.2020.2980477

## II. Problem Definition

The well-known curl–curl problem, considered in this article, can be derived by neglecting displacement currents in Maxwell's system of equations, and introducing the magnetic vector potential $\boldsymbol{A}$ leads to

$$\nabla\times\nu\nabla\times\boldsymbol{A}+\kappa\boldsymbol{A}=\boldsymbol{J}_i,\quad \text{on } \Omega \tag{1}$$

where the parameter $\kappa = \{\xi, \tilde{\gamma}\,\partial/\partial t, j\omega\tilde{\gamma}\}$ determines the analysis type {static, transient, harmonic }and $\nu$ is the magnetic reluctivity. For the magnetostatic case, a small artificial conductivity $\xi$ is applied for regularization purposes, see Section VIII, as well as in the harmonic and transient cases in non-conducting regions, via the definition

$$\tilde{\gamma}=\begin{cases}\gamma, & \text{for } \gamma\neq 0\\ \xi, & \text{for } \gamma = 0\end{cases} \tag{2}$$

where $\gamma$ denotes the electric conductivity. Furthermore, the following interface and boundary conditions have to be fulfilled:

$$\begin{aligned}\boldsymbol{n}_1\times\boldsymbol{A}_1&=-\boldsymbol{n}_2\times\boldsymbol{A}_2,\ \text{on } \Gamma_\mathrm{I}\\ \nu_1\nabla\times\boldsymbol{A}_1\times\boldsymbol{n}_1&=-\nu_2\nabla\times\boldsymbol{A}_2\times\boldsymbol{n}_2,\ \text{on } \Gamma_\mathrm{I}\\ \boldsymbol{n}\times\boldsymbol{A}&=0,\ \text{on } \partial\Omega\end{aligned} \tag{3}$$

which are of importance when defining the jump and average operators in Section III.

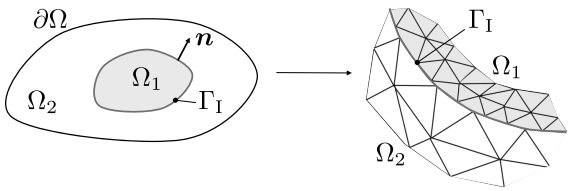


Fig. 1. Computational domain with two subregions $\Omega_1$ and $\Omega_2$.

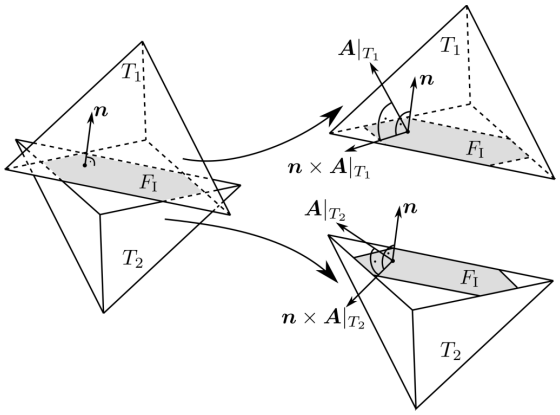


Fig. 2. Quantities on both sides of the interface facet $F_I$, corresponding to the adjacent elements $T_1$ and $T_2$, needed for the definition of the jump operators.

## III. Domain and Operator Definitions

The considered problem from Section II is defined on the global computational domain $\Omega$, consisting of two disjoint and non-overlapping domains with closure $\overline{\Omega} = \overline{\Omega}_1 \cup \overline{\Omega}_2$. Let us denote the outer boundary $\partial\Omega = \Gamma_e \cup \Gamma_n$ as the union of the essential boundary $\Gamma_e$ and natural boundary $\Gamma_n$. Both subdomains share a common interface $\Gamma_I = (\overline{\Omega}_1 \backslash \Omega_1) \cap (\overline{\Omega}_2 \backslash \Omega_2)$, as shown in Fig. 1.

The physical domain $\Omega$ is discretized into non-overlapping elements $T \in \mathcal{T}_h$ of the mesh $\mathcal{T}_h$ (see Fig. 1). A face $F$ is a facet of element $T$ and part of the set of all faces $F \in \mathcal{F}_h$. In 3-D, $\mathcal{F}_h$ are faces (triangles or quadrilaterals), whereas in 2-D, $\mathcal{F}_h$ consists of lines.

The jump $[\cdot]$ of the solution $\boldsymbol{A}$ and its tangential component, respectively, across the common interface facet $F_I$ of two, not necessarily conforming, elements $T_1$ and $T_2$, depicted in Fig. 2, are defined as follows:

$$\begin{aligned} [\boldsymbol{A}] &:= \boldsymbol{A}|_{T_1} - \boldsymbol{A}|_{T_2} \\ [\boldsymbol{n} \times \boldsymbol{A}] &:= \boldsymbol{n} \times \boldsymbol{A}|_{T_1} - \boldsymbol{n} \times \boldsymbol{A}|_{T_2} \end{aligned} \tag{4}$$

with $\boldsymbol{n}$ as the common normal vector (either $\boldsymbol{n}_1$ or $\boldsymbol{n}_2$). Furthermore, the average operator $\{\cdot\}$ is defined as follows:

$$\{\boldsymbol{A}\}_\nu := \tilde{\nu}_1 \boldsymbol{A}|_{T_1} + \tilde{\nu}_2 \boldsymbol{A}|_{T_2} \tag{5}$$

with the coefficients for the average and jump operators, based on [13]

$$\tilde{\nu}_1 := \frac{\nu_1}{\nu_1 + \nu_2}, \quad \tilde{\nu}_2 := \frac{\nu_2}{\nu_1 + \nu_2} \tag{6}$$

where $\nu_1$ and $\nu_2$ denote the magnetic reluctivity of domains $\Omega_1$ and $\Omega_2$.

## IV. Interior Penalty Approach

Before Nitsche's idea [8] of penalizing the jump of quantities over an interface can be applied, the following function space needs to be defined for the DG version of the eddy current problem, based on [14]:

$$H(\text{curl}, \mathcal{T}_h) := \{\boldsymbol{A} \in (L^2(\Omega))^3 : \forall T \in \mathcal{T}_h : \boldsymbol{A}|_T \in H(\text{curl}, T)\} \tag{7}$$

which means that the global solution $\boldsymbol{A}$ is in $(L_2(\Omega))^3$, whereas the local element solution is in $H(\text{curl}, T)$, allowing jumps across elements. The standard (conforming FEM) global function space $H(\text{curl}, \Omega)$ is defined as follows:

$$H(\text{curl}, \Omega) := \{\boldsymbol{A} \in (L^2(\Omega))^3 \, : \, \nabla\times\boldsymbol{A} \in (L^2(\Omega))^3\}. \tag{8}$$

Equipped with these definitions and spaces, the IP DG formulation for the curl–curl problem (1) reads as follows: find $\boldsymbol{A}_h \in V_h \subset H(\text{curl}, \mathcal{T}_h)$ such that $\forall \boldsymbol{A}'_h \in V_h$:

$$\begin{aligned} &\sum_{T\in\mathcal{T}_h} \Big( (\nu \nabla\times\boldsymbol{A}_h, \, \nabla\times\boldsymbol{A}'_h)_T + \left(\kappa \boldsymbol{A}_h, \, \boldsymbol{A}'_h\right)_T \Big) \\ &\quad - \sum_{F\in\mathcal{F}_h} \Big( \langle \{\nabla\times\boldsymbol{A}_h \times \boldsymbol{n}\}_\nu, \left[\boldsymbol{A}'_h\right]\rangle_F \\ &\qquad + \langle \epsilon \left\{\nabla\times\boldsymbol{A}'_h \times \boldsymbol{n}\right\}_\nu, \, [\boldsymbol{A}_h]\rangle_F \\ &\qquad + \beta \left\langle \frac{\overline{\nu} p_E^2}{h_E} [\boldsymbol{n} \times \boldsymbol{A}_h], \, \left[\boldsymbol{n} \times \boldsymbol{A}'_h\right] \right\rangle_F \Big) \\ &= \sum_{T\in\mathcal{T}_h} \left(\boldsymbol{J}_i, \, \boldsymbol{A}'_h\right)_T + \sum_{F\in\mathcal{F}_h} \Big( \langle \epsilon \left\{\nabla\times\boldsymbol{A}'_h \times \boldsymbol{n}\right\}_\nu, \, [\boldsymbol{g}_e]\rangle_F \\ &\qquad + \left\langle \frac{\overline{\nu} p_E^2}{h_E} [\boldsymbol{n} \times \boldsymbol{g}_e], \, \left[\boldsymbol{n} \times \boldsymbol{A}'_h\right] \right\rangle_F \Big) \end{aligned} \tag{9}$$

where $(\cdot, \cdot)_T$ and $\langle \cdot, \cdot \rangle_F$ denote the volume and surface integral over element $T$ and surface area $F$, respectively, with a dot product between its arguments,[1] $\beta$ is the penalty factor, and $\boldsymbol{g}_e$ is the prescribed essential boundary values at $\Gamma_e$. The parameter $\epsilon$ is chosen to be $\epsilon = -1$, resulting in a symmetric interior penalty Galerkin method (SIPG) method. At this point, Remark 1 from [11] can be used, which shows that if $V_h \subset H(\text{curl}, \Omega)$, all jumps across interior faces are vanishing, which is summarized in the following theorem.

*Theorem 1 (Vanishing Jumps):* Assume $\boldsymbol{A}_h \in H(\text{curl}, \mathcal{T}_h)$. For a conforming mesh (respectively, no discontinuities in $\boldsymbol{n} \times \boldsymbol{A}$) we even have $\boldsymbol{A} \in H(\text{curl}, \Omega)$, which is equivalent to no tangential jumps $[\boldsymbol{n} \times \boldsymbol{A}] = 0$ across interior facets.

With this result, we can recover a classical FEM (conforming mesh) formulation by setting the internal tangential jumps to zero. The only remaining jumps occur at the essential boundary of the considered domains, which are now incorporated weakly.

[1]For example, $(\boldsymbol{a}, \boldsymbol{b})_T = \int_T \boldsymbol{a} \cdot \boldsymbol{b} \, dx$ and $\langle \boldsymbol{a}, \boldsymbol{b} \rangle_F = \int_F \boldsymbol{a} \cdot \boldsymbol{b} \, ds$, with $\boldsymbol{a}, \boldsymbol{b} \in \mathbb{R}^3$, and $dx$ and $ds$ as an infinitesimal volume and surface element, respectively.

## V. Application to Non-Conforming Interfaces

Let us now consider the domain setup from Fig. 1, where the discretization $\mathcal{T}_h^1$ of $\Omega_1$ and $\mathcal{T}_h^2$ of $\Omega_2$, with $\mathcal{T}_h = \mathcal{T}_h^1 \cup \mathcal{T}_h^2$ are conforming in their interior but non-conforming across their common interface $\Gamma_I$. The global set of facets is now split into purely interior facets $\mathcal{F}_h^i$, interface facets $\mathcal{F}_h^I$, and essential facets (Dirichlet boundaries) $\mathcal{F}_h^e$. As in Section IV, the broken Sobolev space $H(\text{curl}, \mathcal{T}_h)$ is used, as well as the fact (from Theorem 1) that there are no tangential jumps across purely interior facets $\mathcal{F}_h^i$. The solution on both subdomains is now in $H(\text{curl}, \Omega_i)$ for $i = \{1, 2\}$. Based on (9), the weak form of the general non-conforming interface problem can then be written as follows: find $\boldsymbol{A}_h \in W_h := \{\boldsymbol{A} \in (L^2(\Omega))^3 : \forall T \in \mathcal{T}_h : \boldsymbol{A}_h|_T \in \mathcal{N}_k^{I,II}$ and $\boldsymbol{A}_h \in V_h^{I,II}$ on $\Omega_\text{i}$, for i $\in \{1, 2\}\}$ such that $\forall \boldsymbol{A}'_h \in W_h$

$$\begin{aligned}
&\sum_{T\in\mathcal{T}_h}\Big(\big(\nu\nabla\times\boldsymbol{A}_h,\ \nabla\times\boldsymbol{A}'_h\big)_T + \big(\kappa\boldsymbol{A}_h,\ \boldsymbol{A}'_h\big)_T\Big) \\
&\quad - \sum_{F\in\mathcal{F}_h^I}\Big(\langle\{\nabla\times\boldsymbol{A}_h\times\boldsymbol{n}\}_\nu, \big[\boldsymbol{A}'_h\big]\rangle_F \\
&\qquad + \langle\epsilon\big\{\nabla\times\boldsymbol{A}'_h\times\boldsymbol{n}\big\}_\nu,\ [\boldsymbol{A}_h]\rangle_F \\
&\qquad + \beta\Big\langle\frac{\overline{\nu}p_E^2}{h_E}[\boldsymbol{n}\times\boldsymbol{A}_h],\ \big[\boldsymbol{n}\times\boldsymbol{A}'_h\big]\Big\rangle_F\Big) \\
&= \sum_{T\in\mathcal{T}_h}(\boldsymbol{J}_i,\ \boldsymbol{A}'_h)_T + \sum_{F\in\mathcal{F}_h^e}\Big(\langle\epsilon\big\{\nabla\times\boldsymbol{A}'_h\times\boldsymbol{n}\big\}_\nu,\ [\boldsymbol{g}_e]\rangle_F \\
&\qquad + \Big\langle\beta\frac{\overline{\nu}p_E^2}{h_E}[\boldsymbol{n}\times\boldsymbol{g}_e],\ \big[\boldsymbol{n}\times\boldsymbol{A}'_h\big]\Big\rangle_F\Big).
\end{aligned} \tag{10}$$

The used approximation space is curl-conforming in whole $\Omega_1$ and $\Omega_2$ but broken across the interface facets $\mathcal{F}_h^I$ at the interface $\Gamma_I$. To approximate the solution in the two conforming domains, $H(\text{curl})$-conforming Nédélec edge elements are used.

## VI. Approximation Error Estimates

The approximation error for edge elements of the first kind was already derived in Theorem 2 of [11], which is briefly recapitulated in the following.

*Theorem 2 (Approximation Error Estimates for Non-Conforming Edge FEM of First Kind:)* Assume the exact solution $\boldsymbol{A} \in H(\text{curl}, \Omega) \cap (H^s(\Omega_i))^3$ and $\nabla\times\boldsymbol{A} \in (H^s(\Omega_i))^3$ for $i \in \{1, 2\}$, with $1 \leq s \leq k \in \mathbb{N}^+ \setminus \{0, 1\}$, then follows:

$$\begin{aligned}
&||\boldsymbol{A} - \tilde{\boldsymbol{r}}_h\boldsymbol{A}||_\text{SWIP} \\
&\qquad < Ch_E^{s-1}\sum_{i\in\{1,2\}}\big(||\boldsymbol{A}||_{(H^s(\Omega_i))^3} + ||\nabla\times\boldsymbol{A}||_{(H^s(\Omega_i))^3}\big)
\end{aligned} \tag{11}$$

with a constant $C$, independent of $h_E$, $p_E$, and $\nu$, denoting the element size, element order, and reluctivity, respectively, together with $\tilde{\boldsymbol{r}}_h$ as the projection operator with $\boldsymbol{A} \mapsto (\boldsymbol{r}_h\boldsymbol{A}|_{\Omega_1}, \boldsymbol{r}_h\boldsymbol{A}|_{\Omega_2})$.

The symmetric weighted interior penalty (SWIP) norm, used in the above theorem, is defined as follows:

$$\begin{aligned}
||\boldsymbol{A} - \tilde{\boldsymbol{r}}_h\boldsymbol{A}||^2_\text{SWIP} &= \underbrace{||\nu\nabla\times(\boldsymbol{A} - \tilde{r}_h\boldsymbol{A})||^2_{(L^2(\Omega))^3}}_{T_1} \\
&\quad + \underbrace{\tilde{\gamma}\,||\nu(\boldsymbol{A} - \tilde{r}_h\boldsymbol{A})||^2_{(L^2(\Omega))^3}}_{T_2} \\
&\quad + \underbrace{\sum_{F\in\mathcal{F}_h^I}\beta\frac{\overline{\nu}p_E^2}{h_E}||[\boldsymbol{A} - \tilde{r}_h\boldsymbol{A}]]||^2_{(L^2(\Omega))^3}}_{T_3} \\
&\quad + \underbrace{\sum_{T\in\mathcal{T}_h}h_E||\nu\nabla\times(\boldsymbol{A} - \tilde{\boldsymbol{r}}_h\boldsymbol{A})||^2_{(L^2(\Omega))^3}}_{T_4}
\end{aligned} \tag{12}$$

where the critical (third) term $T_3$ can be bounded by the expression in (11). This term is critical because the mesh size parameter $h_E$ has an exponent of element order minus one, which increases the error for lowest order edge elements $s = 1$ of the first kind when performing h-refinement. The other terms scale with positive orders, and thus, the error decreases when refining the mesh.

The important implication of the last theorem is that for the lowest order Nédélec elements of the first kind, convergence should only be obtained if the order $s$ is larger than 1. In Section VIII, however, it is heuristically shown that the sharpness of this theorem depends on the actual problem and setup of the computational domain. At this point, it is important to note that from the practical (application-oriented) point of view, it cannot be claimed that the solution only has global convergence $\mathcal{O}(h_E^{s-1})$ because the approximation error (11) is only striking on the non-conforming interface. If the solution is concentrated on the interface or significantly depends on it, the convergence will tend toward $\mathcal{O}(h_E^{s-1})$ (observed in [11]), whereas for solutions with no concentration on the interface, higher orders of convergence are achieved, discussed in Section VIII. Furthermore, there seems to be a dependence on the number of dof on the interface, compared to the dofs in the conforming regions. If this ratio is small (a small number of dofs on the interface), a higher order of convergence is observed, also presented in Section VIII. It is also important to state that the above error estimate only holds for Nédélec elements of the first kind.

The approximation error estimate for non-conforming edge elements of the second kind can be obtained similar to Theorem 2, with the following theorem as the outcome.

*Theorem 3 (Approximation Error Estimates for Non-Conforming Edge FEM of Second Kind:)* Assume the exact solution $\boldsymbol{A} \in H(\text{curl}, \Omega) \cap (H^s(\Omega_i))^3$ for $i \in \{1, 2\}$ with integer $1 \leq s \leq k$, then follows:

$$||\boldsymbol{A} - \tilde{r}_h^{II}\boldsymbol{A}||_\text{SWIP} < Ch_E^s\sum_{i\in\{1,2\}}||\boldsymbol{A}||_{(H^{s+1}(\Omega_i))^3} \tag{13}$$

with a constant $C$, independent of $h_E$, $p_E$, and $\nu$.

The full proof of this theorem is neglected in this article because the first two terms of (13), as well as the last one,

can be bounded by using the same method as in [11]. For the third term in (12), an important theorem in [15] was used to bound it and obtain an order of convergence, which coincides with the polynomial order of the element-basis functions. This is necessary because edge elements of the second kind consist of full first-order polynomials, due to the included gradient fields, compared to edge elements of the first kind, consisting only of incomplete polynomials. We can conclude that by using edge elements of the second kind, the order of convergence is increased by one, which circumvents the problem of the third term in Theorem 2 and ensures convergence, which is observed in Section VIII.

## VII. Implementation Aspects

A technical difficulty, which arises when considering the surface integration terms in (10), is that the integration has to be carried out on the actual interface. In our case, the integration on $F \in \mathcal{F}_h^I$ is carried out on an intersection mesh, consisting of the intersection from $\Gamma_1 = \Gamma_I \cap \partial\Omega_1$ and $\Gamma_2 = \Gamma_I \cap \partial\Omega_2$, schematically depicted in Fig. 2 for a coplanar interface in 3-D. For 2-D simulations and coplanar interfaces, the intersection operation is trivial because it corresponds to performing simple interval checks. On the other hand, for simulations with curved interfaces (2-D or 3-D), it becomes computationally and algorithmically demanding. In this case, the elements have to be projected onto a suitable common line or surface segment before the actual intersection. Our implementation uses the open-source library CGAL [16] to perform polygon intersections and triangulate the resulting intersection mesh, in order to avoid "non-computable" elements (2-D polyhedrons with more than four nodes).

For the remainder of this work, we restrict the intersection to planar interfaces in 3-D (no curvature of the interface elements $\mathcal{F}_h^I$), resulting in triangulated surfaces, which can be represented by Cartesian coordinates. A curved surface approximated with a linear mesh can also be handled with our presented method as long as the mesh elements are linear. For curved coordinates, we refer to [17], which includes a more elaborate derivation, because in non-Cartesian coordinates (curvilinear), one must also take the correct transformation of the tangential components $\boldsymbol{n} \times \boldsymbol{A}$ and the differential operators defined in $H(\text{curl})$, into account.

Once the intersection mesh is found, the integrals over the interface can be considered in terms of standard Gauss quadrature, where the intersection elements are solely used as an auxiliary geometrical entity, acting as a source for integration points on the interface and do not carry any dof by themselves. To numerically compute the interface integrals, the basis functions of both interface sides $\Gamma_1$ and $\Gamma_2$ need to be evaluated at those interface integration points. This operation is only trivial for straight-line elements and linear triangles; in general, it is a nonlinear mapping and needs to be handled with, e.g., a Newton–Raphson algorithm. Since we are only using linear triangulated intersection meshes, the main source of numerical error in our case comes from the integration itself. Because most numerical integration schemes are tailored for a certain kind of reference element and polynomial type, it is useful to over integrate on the intersection mesh in order to take heavily distorted intersection elements into account. This poses a problem because for the numerical integration, all elements are scaled with the determinant of its Jacobian and if they have a high aspect ratio (high distortion), the Jacobian becomes ill-conditioned and the accuracy of its inverse deteriorates.

## VIII. Numerical Example I

In the first example, a purely academic 3-D setup is considered, consisting of two cubic bricks with dimensions 1 m × 1 m × 1 m. In order to study the influence of different mesh combinations and order of elements, both parts are meshed independent of each other, only connected via a nonconforming interface. The lower part is made of iron, with a relative reluctivity $\nu_r = 0.1$ and the upper one modeled as air, with $\nu_r = 1$. The lower brick is excited with a static uniform impressed current density in the $y$-direction of $10^4$ A/m$^2$. We are solving the magnetostatic problem with a small regularization parameter ($\xi = \nu_r \cdot 1 \cdot 10^{-6}$) in order to ensure coercivity but not enough for significantly influencing the result due to the scaling with the reluctivity, which scales the artificial mass term six orders of magnitude smaller than the stiffness term. The global magnetic energy is evaluated by

$$E_{\text{m}} = \frac{1}{2} \sum_{i=1}^{2} \int_{\Omega_i} \boldsymbol{H} \cdot \boldsymbol{B} \tag{14}$$

to obtain an integral quantity, which can be used for the subsequent convergence investigations. It should be noted that both quantities in (14) are derived from the actual solution quantity (magnetic vector potential $\boldsymbol{A}$) via

$$\boldsymbol{B} = \nabla \times \boldsymbol{A}, \quad \boldsymbol{H} = \nu \boldsymbol{B} = \nu \nabla \times \boldsymbol{A}. \tag{15}$$

Since there is no straightforward analytical solution of this problem, we construct the reference solution by meshing both parts (including the interface) in a conform way and perform h-refinement, until the relative difference between the magnetic energy $E_m$ of two refinement steps is smaller than $1 \cdot 10^{-5}$. The field result for the magnetic flux density in both parts is depicted in Fig. 5, where the reluctivity jump across the interface is visible through the kink in the field lines and the much lower magnitude of the magnetic flux density.

In the following, we are introducing a planar nonconforming interface surface between the two bricks and perform h-refinement with different mesh combinations of the lower and upper volume, denoted by *hex–hex* and *tet–tet* for hexahedral (*hex*) and tetrahedral (*tet*) meshes, respectively, on both sides and *hex–tet* and *tet–hex* for the combination of both types. An exemplary mesh, representing the *hex–tet* mesh combination, is depicted in Fig. 3.

*h-Refinement:* In this analysis, two slightly different meshes are considered in the upper and lower bricks, which enable us to create an intersection mesh, consisting of heavily distorted elements with aspect ratios of up to 50:1, depicted for the *tet–tet* interface in Fig. 4. These distorted meshes were constructed to show that the possible source for numerical error (element distortions), identified in Section VII, is not

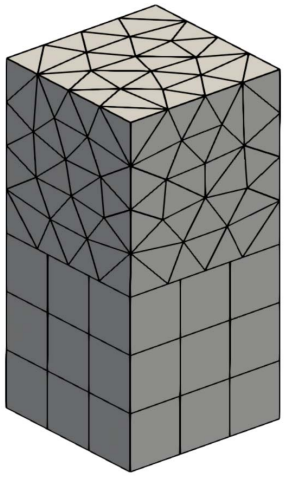

Fig. 3. Exemplary mesh for *hex–tet* mesh combination.

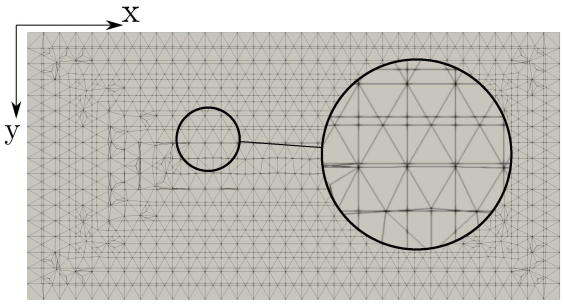


Fig. 4. Exemplary intersection mesh for *tet–tet*.

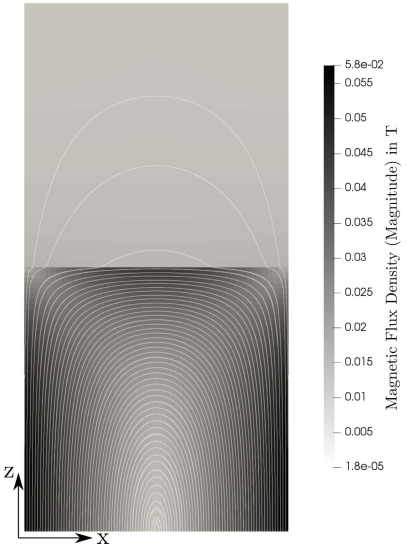


Fig. 5. Magnetic flux density—conform reference solution with depicted traces of the magnetic flux density vector field.

influencing the result in a way, which would prevent convergence.

For all subsequent simulations, only the lowest order edge elements of the first and second kinds are used, and the resulting systems are solved with the direct solver *pardiso* [18]. The reason for the choice of a direct solver is that the

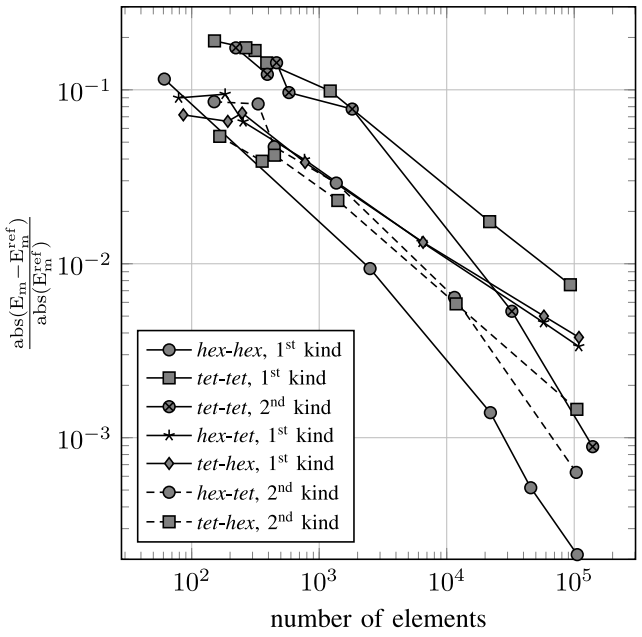


Fig. 6. h-Refinement comparison using lowest order Nédélec elements.

condition number of the resulting system matrices increases quite drastically and one would have to take care to choose a correct preconditioner, when using an iterative solver, which is not within the scope of this work.

In Fig. 6, the convergence behavior of different mesh combinations is depicted. After an initial phase, one can observe a convergence rate of approximately $\mathcal{O}(h^{0.9})$ for *hex–hex* interfaces and edge elements of the first kind. This is already in contrast to (11), which would predict no convergence at all. It seems as if the decisive parameter is the number of dofs on the interface, as already expected, as well as a possible concentration of the solution on the interface. This can be made even more plausible by investigating the dominance of the third term in (12). Since this term only contains contributions on the interface, we can relate its dominance to the ratio of dofs on the non-conforming interface to dofs on the conform domain, as depicted in Fig. 7. Here, we can observe that the contributions from the third term are becoming less dominant, the more refined the mesh is. When looking at the convergence behavior of *tet–tet* as well as *hex–tet* in Fig. 6, we can already see the effect of a larger number of dofs on both sides of the interface because the meshes for *tet–tet* and *hex–tet* include more dofs than the *hex–hex* version. This translates to a decreased convergence rate of about $\mathcal{O}(h^{0.4})$, caused by the increased influence of the third term in (12).

If, however, Nédélec elements of the second kind are used (include gradient fields to obtain complete polynomials), the scaling issue in (11) is avoided and a convergence of $\mathcal{O}(h^1)$ for *hex–tet* as well as *tet–tet* interfaces can be obtained, as expected by Theorem 3.

## IX. Numerical Example II

Since $h$-convergence was already considered in the first example, the aim of the second one is to study the influence of

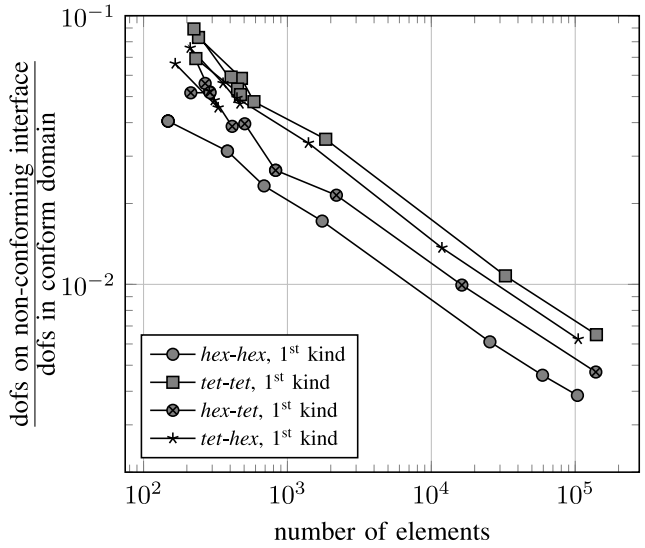


Fig. 7. Comparison of ratio between the number of dof on non-conforming interface and conform domain.

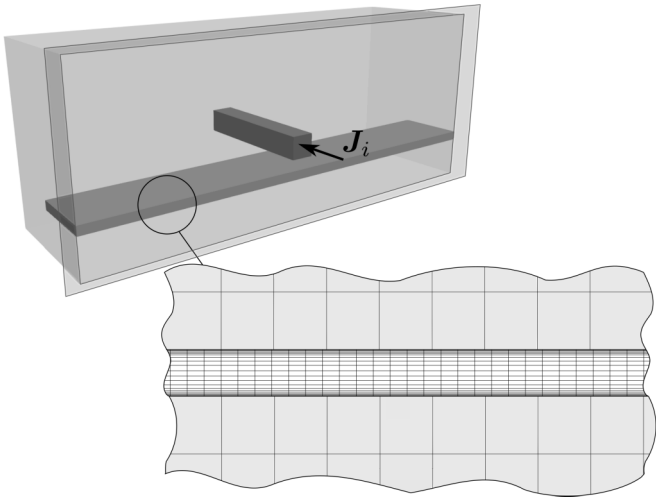


Fig. 8. Inductor setup with non-conforming interface between sheet and air domains.

the penalization- (Nitsche-) parameter on the solution. For this purpose, an induction heating application is considered, where the current carrying inductor is made of copper ($\nu_r = 1$) and harmonically ($f = 8000$ Hz) excited with an impressed current of $1000 \cdot \sin(2\pi\ f\ t)$ A. Beneath the inductor, a steel sheet with an electric conductivity $\gamma = 9.17431 \cdot 10^5\ \Omega^{-1}\ \mathrm{m}^{-1}$ and a relative reluctivity $\nu_r = 0.25$ is placed. Due to the harmonic excitation, eddy currents are induced in the sheet, which have to be resolved with a boundary layer mesh, as depicted in Fig. 8. The surrounding air does not need to be discretized as fine as the steel sheet, and the non-conforming interfaces offer a way to prevent the time-consuming generation of transition layers in the mesh. Furthermore, we only consider half of the problem by using the symmetry plane, depicted as the shaded surface in Fig. 8.

As in the first example, we first construct a conforming mesh and refine it until the relative difference of the global

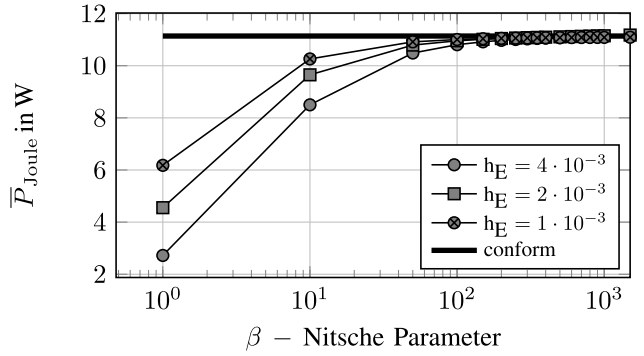


Fig. 9. Convergence of global Joule losses over penalty parameter for three different mesh refinements.

magnetic energy between two subsequent refinement steps is smaller than $1 \cdot 10^{-5}$, which is then considered as the reference solution for the subsequent error evaluations.

*Investigation of Nitsche parameter $\beta$:* In this example, the Nitsche parameter $\beta$ is investigated, which has to be chosen "large enough" [8]. However, from the computational point of view, choosing it too large deteriorates the condition of the resulting system matrix. In [19], it is stated that $\beta$ can be varied in a large range, without a significant impact on the accuracy of the solution and condition number of the system matrix, whereas only nodal elements in $H^1$ were investigated. In the following, we also observe similar behavior with edge elements in $H(\mathrm{curl})$.

Since we are considering this eddy current problem in the frequency domain, we use the period averaged eddy current losses $\overline{P}_{\mathrm{Joule}}$ for the convergence evaluation, which can be derived from the harmonic solution $\hat{\boldsymbol{A}}$ by

$$\overline{P}_{\mathrm{Joule}} = \sum_{i \in \Theta} \int_{\Omega_i} \gamma\, \frac{1}{2} \mathrm{Re}(\hat{\boldsymbol{J}}^* \cdot \hat{\boldsymbol{E}}) \tag{16}$$

where $\Theta = \{\mathrm{sheet}, \mathrm{air}, \mathrm{inductor}\}$, $T$ is the period length, $\omega$ is the angular frequency, $\hat{\boldsymbol{E}}$ is the electric field intensity, corresponding to the magnetic vector potential via $\hat{\boldsymbol{E}} = -j\omega\hat{\boldsymbol{A}}$, $\hat{\boldsymbol{J}}$ is the current density, and $\hat{\boldsymbol{J}}^*$ is its conjugate complex.

In Fig. 9, the dependence of $\overline{P}_{\mathrm{Joule}}$ on the Nitsche parameter $\beta$ is shown for three different mesh sizes, where the straight horizontal line depicts the conform reference solution. It clearly shows the expected behavior of converging toward the reference solution for increasing the Nitsche parameter. If the parameter is increased to values larger than $5 \cdot 10^3$, the deviation increases again, most likely because of the highly ill-conditioned system matrix with condition numbers larger than $1 \cdot 10^{14}$.

## X. Conclusion

In this article, the derivation of non-conforming interfaces for edge elements in $H(\mathrm{curl})$ was presented. The starting point was an interior penalty discontinuous Galerkin description of the general curl–curl problem, obtained from Maxwell's equations, with the computational domain consisting of conforming parts, "glued" together along with non-conforming interfaces. For the conforming parts, a classical continuous FE discretization was applied and the jump of the solution

was taken care of via penalty surface integral terms on the interface.

With this Nitsche approach, no additional unknowns are introduced, as it would be the case for Lagrange multipliers in Mortar methods. On the other hand, the correct choice of the penalty parameter $\beta$ (citing the original article from Nitsche [8], it has to be chosen "large enough") leaves room for controversial discussions [20], because one has to choose the parameter as large as possible, without having a significant degradation of the condition number of the system matrix. In the application examples in Sections VIII and IX, it could furthermore be shown that the penalization- (Nitsche-) parameter can be chosen in a relatively large range (between 400 and 4500), without deteriorating the solution significantly.

It was heuristically shown that the approximation error estimate (11) does depend on the actual problem, where the interface is located and which kind of elements are used. When using the lowest order edge elements of the first kind, one has to keep in mind that a large ratio of unknowns on the non-conforming interface to unknowns on the conform region can deteriorate the convergence. This does not occur for edge elements of the second kind, whereas the number of unknowns is increased, compared to elements of the first kind.

In the next step, the presented methodology will be applied to non-planar interfaces, where special techniques for the intersection mesh generation are needed, as well as for sliding interfaces, which can then be used for rotor–stator simulations of motors.

## REFERENCES


[1] G. J. Wallinger and O. Biro, "3-D FE method analysis of static fields for non-conforming meshes with second-order node-based elements," *IEEE Trans. Magn.*, vol. 52, no. 3, pp. 1–4, Mar. 2016.

[2] G. J. Wallinger and O. Biro, "Improved coupling strategy to cover curved FE-facets in the non-conforming mesh method," *IEEE Trans. Magn.*, vol. 55, no. 6, pp. 1–4, Jun. 2019.

[3] C. Bernardi, N. Debit, and Y. Maday, "Coupling finite element and spectral methods: First results," *Math. Comput.*, vol. 54, no. 189, pp. 21–39, Jan. 1990.

[4] J. Gopalakrishnan and J. E. Pasciak, "Multigrid for the mortar finite element method," *SIAM J. Numer. Anal.*, vol. 37, no. 3, pp. 1029–1052, Jan. 2000.

[5] A. Razek, Y. Maday, A. Buffa, L. Santandrea, E. Bouillault, and F. Rapetti, "Calculation of eddy currents with edge elements on non-matching grids in moving structures," *IEEE Trans. Magn.*, vol. 36, no. 4, pp. 1351–1355, Jul. 2000.

[6] S. Boehmer, E. Lange, and K. Hameyer, "Non-conforming sliding interfaces for relative motion in 3D finite element analysis of electrical machines by magnetic scalar potential formulation without cuts," *IEEE Trans. Magn.*, vol. 49, no. 5, pp. 1833–1836, May 2013.

[7] S. Bohmer, C. Kruttgen, B. Riemer, and K. Hameyer, "Eddy currents and non-conforming sliding interfaces for motion in 3-D finite element analysis of electrical machines," *IEEE Trans. Magn.*, vol. 51, no. 3, pp. 1–4, Mar. 2015.

[8] J. Nitsche, "Über ein Variationsprinzip zur Lösung von Dirichlet-Problemen bei Verwendung von Teilräumen, die keinen Randbedingungen unterworfen sind," *Abhandlungen aus dem Mathematischen Seminar der Universität Hamburg*, vol. 36, no. 1, pp. 9–15, Jul. 1971.

[9] P. Alotto, A. Bertoni, I. Perugia, and D. Schotzau, "Efficient use of the local discontinuous Galerkin method for meshes sliding on a circular boundary," *IEEE Trans. Magn.*, vol. 38, no. 2, pp. 405–408, Mar. 2002.

[10] I. Perugia and D. Schötzau, "The $hp$-local discontinuous Galerkin method for low-frequency time-harmonic Maxwell equations," *Math. Comput.*, vol. 72, no. 243, pp. 1179–1215, Oct. 2002.

[11] R. Casagrande, R. Hiptmair, and J. Ostrowski, "An a priori error estimate for interior penalty discretizations of the curl-curl operator on non-conforming meshes," *J. Math. Ind.*, vol. 6, no. 1, p. 4, Dec. 2016.

[12] S. Zaglmayr, "High order finite element methods for electromagnetic field computation," Ph.D. dissertation, Inst. Numer. Math., Johannes Kepler Univ., Linz, Austria, Aug. 2006.

[13] D. Maksymilian, "On discontinuous Galerkin methods for elliptic problems with discontinuous coefficients," *Comput. Methods Appl. Math.*, vol. 3, no. 1, pp. 76–85, 2003.

[14] M. Neumüller, "Space-time methods: Fast solvers and applications," Ph.D. dissertation, Inst. Comput. Math., TU Graz, Graz, Austria, 2013.

[15] L. Zhong, "Optimal error estimates for nedelec edge elements for time-harmonic Maxwell's equations," *J. Comput. Math.*, vol. 27, no. 5, pp. 563–572, Jun. 2009.

[16] The CGAL Project. (2018). *CGAL User and Reference Manual, 4.13 ed. CGAL Editorial Board*. [Online]. Available: https://doc.cgal.org/4.13/Manual/packages.html

[17] P. J. Matuszyk and L. F. Demkowicz, "Parametric finite elements, exact sequences and perfectly matched layers," *Comput. Mech.*, vol. 51, no. 1, pp. 35–45, Jan. 2013.

[18] O. Schenk, K. Gärtner, W. Fichtner, and A. Stricker, "PARDISO: A high-performance serial and parallel sparse linear solver in semiconductor device simulation," *Future Gener. Comput. Syst.*, vol. 18, no. 1, pp. 69–78, Sep. 2001.

[19] M. Kaltenbacher, *Numerical Simulation of Mechatronic Sensors and Actuators: Finite Elements for Computational Multiphysics*. Berlin, Germany: Springer-Verlag, 2015.

[20] D. N. Arnold, F. Brezzi, B. Cockburn, and L. D. Marini, "Unified analysis of discontinuous Galerkin methods for elliptic problems," *SIAM J. Numer. Anal.*, vol. 39, no. 5, pp. 1749–1779, Jan. 2002.